UTD Vertex Diffraction Coefficient for the Scattering by Perfectly Conducting Faceted Structures

Matteo Albani, *Member, IEEE*, Filippo Capolino, *Senior Member, IEEE*, Giorgio Carluccio, and Stefano Maci, *Fellow, IEEE*

This paper is dedicated to our former Professor and friend Roberto Tiberio, who introduced us to the theory of spectral representations and diffraction. It is under his guidance that our initial research on this topic started, and our approach to any diffraction matter reflects the long term vision we have learned from him.

***Abstract*—A uniform high-frequency description is presented for vertex (tip) diffraction at the tip of a pyramid, for source and observation points at finite distance from the tip. This provides an effective engineering tool able to describe the field scattered by a perfectly conducting faceted structure made by interconnected flat plates within a uniform theory of diffraction (UTD) framework. Despite the adopted approximation, the proposed closed form expression for the vertex diffracted ray is able to compensate for the discontinuities of the field predicted by standard UTD, i.e., geometrical optics combined with the UTD wedge diffracted rays. The present formulation leads to a uniform first order asymptotic field in all the transition regions of the tip diffracted field. The final analytical expression is cast in a UTD framework by introducing appropriate transition functions containing Generalized Fresnel Integrals. The effectiveness and accuracy of the solution is checked both through analytical limits and by comparison with numerical results provided by a full wave method of moments analysis.**

***Index Terms*—Asymptotic diffraction theory, geometrical theory of diffraction, radar cross section (RCS), scattering, uniform theory of diffraction (UTD), vertex diffraction.**

I. Introduction

THE description of the electromagnetic field in terms of rays is a very effective tool for modeling complex environments at high frequencies. This technique has been thoroughly employed for the prediction of the radar cross section (RCS) of complex targets or for the computation of radiation characteristics of antennas in their operating environments (on board of aircraft, ships, satellites, etc.). Recently, the same technique has been adopted also for the deterministic prediction of the field propagation in wireless applications for urban and indoor scenarios. A commonly used general approach consists in representing arbitrary scatterers with faceted surfaces, constituted by interconnecting flat triangular (or polyhedral) flat plates. At their junctions, plates form wedges and pyramid vertices (tips); when a plate is isolated and its sides are not connected to other plates, it contains half-plane edges and plane-angular-sector vertices. The plane-angular-sector can be regarded as a particular case of the pyramid geometry. In the faceted representation of scatterers, the leading asymptotic contributions are the geometrical optics (GO) direct and reflected rays of k^0 asymptotic order, where k is the wavenumber. Wedge or edge diffracted rays are added as prescribed by the uniform theory of diffraction (UTD) [1], thus augmenting the solution the asymptotic order $k^{-1/2}$. This way, the uniform description of the transitional behavior of the wedge diffracted field restores the continuity of the total predicted field across the GO shadow boundaries (SBs). However, this kind of description is not satisfactory when the observation point lies near the wedge singly-diffracted field SBs, i.e., those surfaces across which a wedge singly-diffracted ray abruptly appears/disappears, thus resulting in an unphysical field discontinuity. Furthermore, the UTD (GO+wedge) field description is not accurate in shadow regions where no GO or wedge diffracted ray occur, thus resulting in a vanishing total field. For the above mentioned reasons, higher order contributions must be added; namely, vertex and doubly diffracted contributions. These contributions augment the asymptotic solution to the k^{-1} order out of their transition regions, and their uniform description restores the continuity of the field at the wedge singly-diffracted ray SBs. In this paper we focus our attention on vertex diffracted contributions. Uniform description of edge doubly diffracted rays can be found in [2]–[5], and in the references therein contained.

The diffraction at the vertex of a plane angular sector admits a solution in terms of a spherical wave series expansion [6]–[13], which however involves the calculation of eigenfunctions and exhibits a critical convergence in the plane-wave far-field regime, and it is therefore not suitable for asymptotic ray description. In [14], [15] a plane wave spectrum solution for the quarterplane was proposed, whose form is amenable for asymptotics, as that developed in [16]. Though it was claimed as an exact solution, in [17] it was proved that it does not fulfill the boundary conditions. To overcome these problems, other heuristic solutions were proposed for the asymptotic ray description of vertex diffracted rays with limitation to plane angular sectors [18]–[24]. The pioneering work [18], which is still widely applied, heuristically describe the vertex diffracted ray

Manuscript received June 24, 2009. First published July 14, 2009; current version published December 01, 2009.

M. Albani, G. Carluccio, and S. Maci are with the Department of Information Engineering, University of Siena, Siena 53100, Italy (e-mail: matteo.albani@dii.unisi.it).

F. Capolino is with the Department of Electrical Engineering and Computer Science, University of California, Irvine, CA 92697 USA.

Color versions of one or more of the figures in this paper are available online at http://ieeexplore.ieee.org.

Digital Object Identifier 10.1109/TAP.2009.2027455

transitions simply using products of UTD transition functions (Fresnel functions). This approach, despite its simplicity does not reproduce the correct transitional behavior as highlighted in [25]. Therefore, other solutions ([19], [20]) were developed by using the generalized Fresnel integral (GFI) [26]–[28] as a special function describing the vertex ray transition. Other works [22], [23] also included the double edge diffraction in the vertex formulation to augment its accuracy. Plane angular sector fringe currents (to augment physical optics) were derived in [21] with a hybrid method of moments approach and in [24] by using the incremental theory of diffraction [34].

As the pyramid vertex diffraction is concerned, an exact formulation was proposed in [29], [30] by resorting to hybrid numerical-analytical approach, which however does not provide a uniform closed form solution as required in a UTD framework.

Therefore, an effective uniform, closed form asymptotic UTD solution for the diffraction by the vertex of a pyramid is still not available in the literature, thus motivating the present study.

The present formulation is outlined in the following. Section II presents the scalar solution of the proper canonical problem, i.e., a pyramid of infinite extent, composed by an arbitrary number of edges confluent at the tip, with either soft or hard boundary conditions imposed on its faces. By using an adaptation of the method explained in [31], the field is rigorously written in terms of integrals along the edges of the pyramid of the so called Miyamoto-Wolf vector potential [32]. This potential is known only for certain canonical structures, like an infinite wedge. The expression for the Miyamoto-Wolf vector potential is not known for the pyramidal geometry considered in this paper, thus requiring some approximations. To this end, the Miyamoto-Wolf unknown vector potential is interpreted as an alignment of *incremental field contributions*, and its expression is locally approximated by using the known vector potential of the wedge geometry [31]. This vector potential is coincident with that provided by the scalar version of the ITD. The integrals along the semi-infinite edges are then asymptotically evaluated in a uniform fashion, providing the expression of the vertex diffracted field which is cast in a UTD format by introducing a proper transition function involving the GFI [26]–[28]. Section III discusses the behavior of the scalar solution focusing on transition regions. In particular we analyze analytically the single and double transition behavior of the uniform vertex diffracted field expression. In Section IV we specialize the result to the cases of plane wave incidence and far field observation, with particular attention to the RCS case.

The extension to the electromagnetic case is provided in Section V by using typical ray optic approximation as that used in the UTD [1]. Numerical examples showing the effectiveness of our proposed vertex diffracted field expression, and a comparison with the method of moments is shown in Section VI. In this section we clearly show that the use of the UTD field expressions (GO + edge diffraction) leads to non physical field jump discontinuities that are repaired by the vertex diffracted field.

II. Scalar Formulation

Consider an infinite pyramid as in Fig. 1, with M edges and M faces on which either *soft* or *hard* boundary conditions are

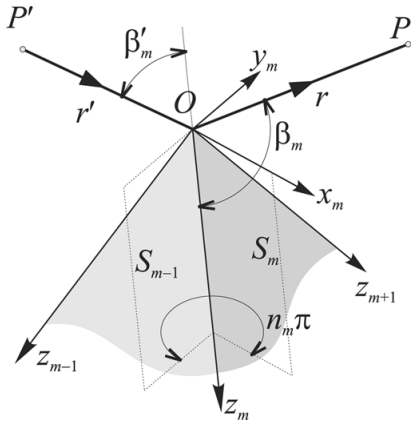

Fig. 1. Pyramid geometry and reference systems centered at the vertex (tip).

assumed. Edges are counted counterclockwise observing the pyramid from the tip (see Fig. 1); the face S_m tagged by m is delimited by edges tagged by m and $m+1$. In our formulation the pyramid is thought of as the superposition of M wedges sharing a common face, all intersecting at the pyramid vertex. It is convenient to introduce a reference system for each edge m, with its origin at the pyramid vertex, its z_m axis along the edge, the x_m axis lying on the half-plane (wedge face) containing the pyramid face S_m, and the y_m axis parallel to the outgoing normal to the face S_m (Fig. 1). The exterior angle of wedge m equals $n_m\pi$, its $\phi_m = 0$ and $\phi_m = n_m\pi$ faces correspond to the pyramid faces S_m and S_{m-1}, respectively.

The pyramid is illuminated by an isotropic scalar spherical wave

$$\Psi^{\text{inc}}(P,P') = \frac{e^{-jkr_{PP'}}}{4\pi r_{PP'}} \tag{1}$$

where $r_{PP'}$ denotes the distance between the point source at P' and the observation point at P. Hereinafter, the distance between two points A and B will be denoted by r_{AB}.. By invoking the Helmholtz-Huygens principle, the field scattered by the pyramid is expressed as the radiation integral over its surface; which is decomposed as the sum of M terms, each relevant to a face m. Hence, the total field is given by the sum of the incident and the scattered fields

$$\Psi^{\text{tot}}(P,P') = \Psi^{\text{inc}}(P,P') + \sum_{m=1}^{M} \iint_{S_m} \mathbf{V}(P,Q,P') \cdot \hat{\mathrm{n}}\, dS \tag{2}$$

where S_m is the surface of the face m, $\hat{\mathrm{n}}$ the unit vector normal to the surface at the integration point Q, and

$$\mathbf{V}(P,Q,P') = \Psi^{\text{tot}}(Q,P')\nabla_Q \frac{e^{-jkr_{PQ}}}{4\pi r_{PQ}} - \frac{e^{-jkr_{PQ}}}{4\pi r_{PQ}} \nabla_Q \Psi^{\text{tot}}(Q,P'). \tag{3}$$

Here and after, bold face symbols denote vectors, whereas unit vectors are denoted by a hat. Since $\nabla_Q \cdot \mathbf{V}(P,Q,P') = 0, \mathbf{V}$ can be expressed through [31], [32]

$$\mathbf{V}(P,Q,P') = \nabla_Q \times \mathbf{W}(P,Q,P') \tag{4}$$

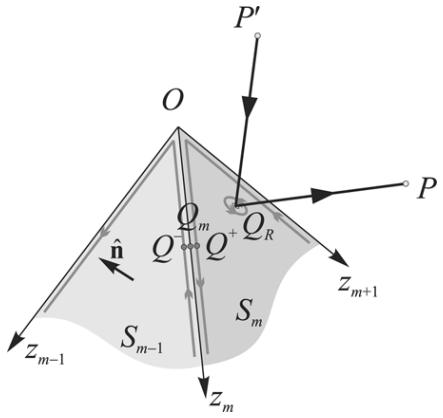

Fig. 2. Reduction of the surface radiation integral on the faces of the pyramid, to line integrals along the edges, by using the Stokes theorem.

where $\mathbf{W}$ is the so-called Miyamoto-Wolf vector potential. In [32], the implicit definition (4) for $\mathbf{W}$ in terms of a differential equation is recast in an explicit integral expression. Using (4) in (2), and applying the Stokes theorem, reduce each term of the summation to a line integral along the border of the surface S_m, i.e., along edges m and $m+1$, plus a residue contribution if a singularity of $\mathbf{W}$ occurs on S_m. As shown in [32], $\mathbf{W}$ is singular, in the Q variable, either at a reflection point Q_R (shown in Fig. 2) on the pyramid surface or at the intersection point between the direct ray and the pyramid surface. Hence, the residue contributions account either for a GO reflected field (Fig. 2) or for minus the incident field in the shadow region. This physical interpretation is further detailed in [32]. This leads to the total field representation

$$\Psi^{\mathrm{tot}}(P,P') = \Psi^{\mathrm{GO}}(P,P') + \Psi^{d}(P,P') \tag{5}$$

where

$$\Psi^{d}(P,P') = \sum_{m=1}^{M} \int_{0}^{\infty} \psi^{d}(P,Q_m,P')\, dz_m \tag{6}$$

is the field diffracted by the pyramid and Ψ^{GO} is obtained by the sum of the incident field Ψ^{inc} (not shadowed by the pyramid) and the above residue contributions, thus recovering the total standard direct and reflected GO terms with their proper existence region (see [1] for example). In (6), the diffracted field is given by [31]

$$\psi^{d}(P,Q_m,P') = \lim_{Q^{\pm}\to Q_m} [\mathbf{W}(P,Q^{+},P') - \mathbf{W}(P,Q^{-},P')] \cdot \hat{\mathbf{z}}_m \tag{7}$$

and the m-sum tags the edges of the pyramid. In (7), the points Q^+ and Q^- lie on face m and $m-1$, respectively, and both approach the integration point Q_m on edge m (Fig. 2); such limit leads to a finite value despite the singular behavior of each of both terms in (7). The evaluation of Ψ^d implies the knowledge of the vector potential $\mathbf{W}$ on the edges of the pyramid, which would require the knowledge of the unknown scattered field Ψ^{tot} [see (3)]. The latter is in general not available in form suitable for asymptotic evaluations. We seek an expression that though approximated is able to solve various problems encountered by engineers when modeling complex structures made of edges and vertexes. We thus approximate $\mathbf{W}$ by the known expression it assumes for the *infinite* wedge problem that fits two contiguous pyramid faces. Due to the localization of high-frequency phenomena, this approximation is accurate for incremental field contributions arising from points far from the tip of the pyramid. Furthermore, the *infinite* wedge potential $\mathbf{W}$ exhibits the appropriate pole singularities, in the Q variable, whose residues reconstruct the GO contributions. Hence, in transition regions of edge-diffracted rays, when the GO points (singularity of $\mathbf{W}$) approach an edge (integration contour), the edge integration provides the appropriate continuity to the GO emergence or disappearance (as in the UTD). This property is still true when the GO point approaches an edge near or even at the tip, i.e., when observing in the simultaneous edge- and tip-diffracted field transition regions. The transition region of an edge-diffracted ray or of a tip-diffracted ray (thoroughly discussed in this paper) is defined as the region where the ray actually changes its spreading factor to match and compensate the appearance or disappearance of another ray species, with lower asymptotic order, at its shadow boundaries. Therefore under the proposed approximation, though the value of $\mathbf{W}$, and in turn that of ψ^d, become inaccurate for points Q near the tip. However, it is important to note that the resulting approximated diffracted field Ψ^d (obtained by integrating in (6) the approximate version of ψ^d on the pyramid edges) still provides the proper jump discontinuity that compensates for the discontinuity of Ψ^{GO} across its planar shadow boundaries, thus preserving the continuity of the resulting approximated total field Ψ^{tot} in (5). This property is crucial for the effectiveness of the final result, and will be analytically verified in the following section, as well numerically in Section VI. The analytic expression for the vector potential $\mathbf{W}$ associated to an infinite straight wedge diffracted field is given in [31], and here reported

$$\psi^{d}(P,Q_m,P') = 2G(\phi_m,\phi'_m,u(z_{Q_m})) \cdot \frac{e^{-jkr_{PQ_m}}}{4\pi r_{PQ_m}} \frac{e^{-jkr_{P'Q_m}}}{4\pi r_{P'Q_m}} \tag{8}$$

where $P \equiv (\rho_m,\phi_m,z_m), P' \equiv (\rho'_m,\phi'_m,z'_m)$, and $Q_m \equiv (0,0,z_{Q_m})$ are the observation point, the source location, and the generic integration point on the edge, respectively, expressed in the edge coordinate system. In (8)

$$\begin{aligned} G(\phi_m,\phi'_m,u_m) = \{&[B(\pi+\phi_m-\phi'_m,u_m) \\ &+ B(\pi-\phi_m+\phi'_m,u_m)] \\ &\mp [B(\pi+\phi_m+\phi'_m,u_m) \\ &+ B(\pi-\phi_m-\phi'_m,u_m)]\} \\ &\cdot U(n_m\pi-\phi_m)U(n_m\pi-\phi'_m) \end{aligned} \tag{9}$$

where the upper (lower) sign applies to the *soft* (*hard*) case and

$$B(\Phi,\alpha) = -\frac{1}{2n}\frac{\sin\left(\frac{\Phi}{n}\right)}{\cos\left(\frac{\Phi}{n}\right)-\cosh\left(\frac{u}{n}\right)} \tag{10}$$

with $n_m\pi$ denoting the wedge exterior angle. The unit step functions U in (9) vanish for negative argument, i.e., if $\phi_m, \phi'_m >$

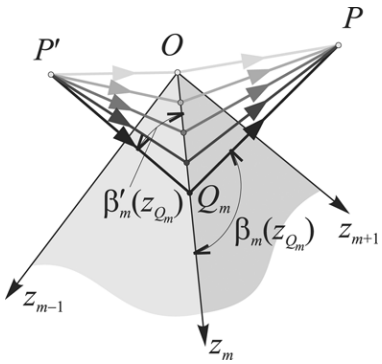

Fig. 3. Distribution of incremental diffracted field contributions along the edge m and local elevation angles. When the argument of β_m and β'_m is not specified, they are referenced to the coordinate system with origin at the tip.

$n_m\pi$. Physically, this happens when the source or the observer is located inside the local infinite wedge. In (8) the parameter u is defined as

$$u_m(z_{Q_m}) = \log\left\{\tan\left[\frac{\beta_m(z_{Q_m})}{2}\right]\right\} - \log\left\{\tan\left[\frac{\beta'_m(z_{Q_m})}{2}\right]\right\} \quad (11)$$

where $\beta_m(z_{Q_m})$ and $\beta'_m(z_{Q_m})$ denote the elevation coordinates of P and P', respectively, measured in a spherical reference system with origin at the point Q_m on the edge (see Fig. 3). (We recall that when the arguments of β_m and β'_m are not specified, these two elevation coordinates are associated to the mth reference system centered at the tip, as in Fig. 1).

In (8), the field at P is interpreted as a spherical wave radiated by an incremental point source at Q_m excited by the illuminating spherical source at P', weighted by the factor 2 G. The representation (6) of the field coincides with the distribution over the semi-infinite edges of the pyramid, of the ITD incremental contributions [33]–[35] relevant to the infinite wedge problem (Fig. 3).

By using the approximation (8) in the exact expression (6) we obtain the approximate integral expression for the pyramid diffracted field

$$\Psi^d(P,P') \approx \sum_{m=1}^{M}\int_0^{\infty} 2G(\phi_m,\phi'_m,u_m(z_{Q_m})) \cdot\frac{e^{-jkr_{PQ_m}}}{4\pi r_{PQ_m}}\frac{e^{-jkr_{P'Q_m}}}{4\pi r_{P'Q_m}}dz_{Q_m} \quad (12)$$

which is suitable for its asymptotic evaluation.

A. Uniform Asymptotic Evaluation

Each m integral in (12) is asymptotically evaluated at its critical points that consist of an end point at $z_{Q_m}=0$ and four pairs of complex conjugate poles in G, each for any B function in (10), whose explicit expression is given in (49) of Appendix A. Furthermore, each integrand in (12) exhibits a stationary phase point at

$$z_{m,s} = \frac{\rho_m z'_m + \rho'_m z_m}{\rho_m + \rho'_m} \quad (13)$$

that satisfies $d(r_{P'Q_m} + r_{PQ_m})/dz_{Q_m} = 0$. This point determines the location of the edge diffraction point (where the edge diffracted ray arises from) on the edge m, that may or may not lie on the integration path from 0 to ∞, i.e., on the actual edge of the pyramid. When the diffraction point lies on the actual edge, i.e., $z_{m,s} > 0$, it leads to the mth edge diffracted field. The asymptotic evaluation at the end-point is associated to the mth contribution to the vertex diffracted field. To isolate saddle point and end-point contributions and prepare the subsequent asymptotic evaluation in terms of edge and vertex field contributions, each integral term of the sum in (12) is exactly split into

$$\Psi^d_m(P,P') = \Psi^{\text{edge}}_m(P,P')U(z_{m,s}) + \Psi^{\text{tip}}_m(P,P') \quad (14)$$

defined as

$$\Psi^{\text{edge}}_m = \int_{-\infty}^{\infty} 2G(\phi_m,\phi'_m,u_m(z_{Q_m}))\frac{e^{-jkr_{PQ_m}}}{4\pi r_{PQ_m}}\frac{e^{-jkr_{P'Q_m}}}{4\pi r_{P'Q_m}}dz_{Q_m} \quad (15)$$

and

$$\Psi^{\text{tip}}_m = \int_0^{-\text{sgn}(z_{s,m})\infty} 2G(\phi_m,\phi'_m,u_m(z_{Q_m})) \cdot\frac{e^{-jkr_{PQ_m}}}{4\pi r_{PQ_m}}\frac{e^{-jkr_{P'Q_m}}}{4\pi r_{P'Q_m}}dz_{Q_m} \quad (16)$$

respectively. Decomposition (14) is interpreted as follows. When $z_{m,s} > 0$, the edge diffraction point lies on the actual part of the semi-infinite pyramid edge, and (14) is split into the wedge contribution (15) and the vertex contribution (16). Conversely, when $z_{m,s} < 0$, the edge diffraction point would lie in the virtual continuation of the actual edge, and thus the edge term (15) does not contribute because of the vanishing unit step function U ($U(z) = 1$ or 0, when $z > 0$ or $z < 0$, respectively) in (14). In this case the diffracted field Ψ^d_m in (14) consists of the vertex contribution Ψ^{tip}_m in (16) only. Therefore, in (14) the wedge diffraction contribution is discontinuous at $z_{m,s} = 0$, i.e., when the diffraction point merges with the vertex of the pyramid; however around this aspect, the vertex contribution (16) undergoes a transition and exhibits a proper discontinuity which restores the continuity of the diffracted field term (14). Note that in (16), the choice of the integration end-point always excludes the stationary phase point from the integration path, therefore the integral is asymptotically dominated only by the end-point, though could be affected by the presence of a nearby saddle point. The sum of all the m contributions leads to the diffracted field

$$\Psi^d(P,P') \approx \sum_{m=1}^{M}\Psi^{\text{edge}}_m(P,P')U(\beta'_m-\beta_m)+\Psi^{\text{tip}}(P,P') \quad (17)$$

in which $\Psi^{\text{tip}}(P,P')$ is the vertex diffracted fields that collects all the m end-point asymptotic contributions. The asymptotic evaluation carried out in Appendix A leads to the wedge diffracted field $\Psi^{\text{edge}}_m(P,P')$ that coincides with the standard

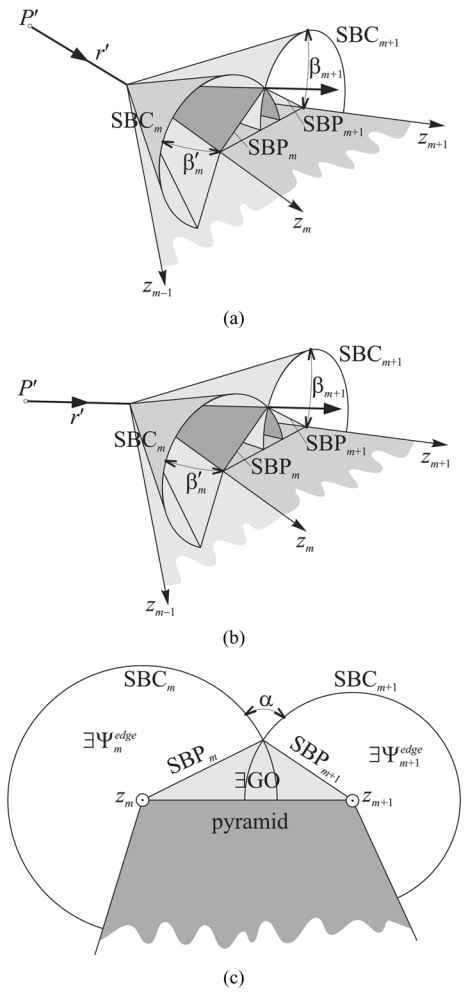

Fig. 4. Geometrical Optics shadow boundary planes (SBPs) and wedge diffraction shadow boundary cones (SBCs) associated to the face S_m of the pyramid; (a) 3D view of reflection SBPs, (b) 3D view of incidence SBPs, and (c) 2D view. In (b) and (c), the GO reflected ray is bounded below the SBPs, the wedge diffracted rays exhibit a transition around the respective SBPs and compensate for the GO field discontinuity. The wedge diffracted rays are bounded inside the respective SBC, the respective term of the vertex diffraction ray exhibit a transition around the SBC compensating for wedge diffracted field discontinuity. SBPs and SBCs all intersect at that aspect (arrow) at which both the GO and the wedge diffracted contributions are discontinuous, while wedge diffracted fields are in transition. Here the vertex diffracted field exhibit a *double* transition able to restore the continuity of the total field. A similar discussion applies to (a).

UTD expression in [1]. By observing that $z_{m,s} = 0$ implies $\beta'_m = \beta_m$, with

$$\beta_m = \cos^{-1}(z_m/r), \quad \beta'_m = \cos^{-1}(-z'_m/r') \tag{18}$$

the unit step function U in (17) bounds the existence of $\Psi_m^{\text{edge}}(P, P')$ into the conical region $\beta_m < \beta'_m$ shown in Fig. 4.

Note that here, the observer r, β_m, z_m and source r', β'_m, z'_m coordinates are associated to the mth reference system centered at the tip O (Fig. 1). It implies that the wedge diffracted field contribution abruptly vanishes or appears at the Shadow Boundary Cone (SBC) $\beta'_m = \beta_m$, for which the UTD edge diffraction point $z_{m,s}$ lies at the pyramid tip.

The uniform asymptotic evaluation for the end-point contribution related to the integral along the mth edge is carried out in Appendix A and leads to the vertex diffracted field expression

$$\Psi_m^{\text{tip}} = \Psi^{\text{inc}}(O, P') D_m^{\text{tip}} \frac{e^{-jkr}}{r} \tag{19}$$

in which $\Psi^{\text{inc}}(O, P') = e^{-jkr'}/(4\pi r')$ is the incident field at the pyramid tip O. Then, by summing all the contributions belonging to all the edges, one obtains the total vertex diffracted field $\Psi^{\text{tip}} = \sum_{m=1}^{M} \Psi_m^{\text{tip}}$, which is cast in the UTD format

$$\Psi^{\text{tip}}(P, P') = \Psi^{\text{inc}}(O, P') D^{\text{tip}} \frac{e^{-jkr}}{r} \tag{20}$$

where we have highlighted the spherical wave arising from all the edge truncations and the vertex diffraction coefficient is

$$D^{\text{tip}} = \sum_{m=1}^{M} D_m^{\text{tip}}. \tag{21}$$

The expression for each D_m^{tip} is given in (22)

$$\begin{aligned} D_m^{\text{tip}} = {} & \frac{1}{2jk\pi(\cos\beta'_m - \cos\beta_m)} \\ & \cdot \Big\{ \Big[B\big(\pi + (\phi_m - \phi'_m), u_m\big) T_{\text{GFI}}\big(b_m, a_m^+(\phi_m - \phi'_m)\big) \\ & + B\big(\pi - (\phi_m - \phi'_m), u_m\big) T_{\text{GFI}}\big(b_m, a_m^-(\phi_m - \phi'_m)\big) \Big] \\ & \mp \big[B\big(\pi + (\phi_m + \phi'_m), u_m\big) T_{\text{GFI}}\big(b_m, a_m^+(\phi_m + \phi'_m)\big) \\ & + B\big(\pi - (\phi_m + \phi'_m), u_m\big) T_{\text{GFI}}\big(b_m, a_m^-(\phi_m + \phi'_m)\big) \big] \Big\} \\ & \cdot U(n_m\pi - \phi_m) U(n_m\pi - \phi'_m) \end{aligned} \tag{22}$$

where the upper (lower) sign applies to the *soft* (*hard*) case and the "Rubinowicz parameter" is

$$u_m = u(0) = \log\left[\tan\frac{\beta_m}{2}\right] - \log\left[\tan\frac{\beta'_m}{2}\right]. \tag{23}$$

In (22), the transition function T_{GFI} is a GFI properly normalized (Section III.A) as

$$T_{\text{GFI}}(b, a) = 2j\sqrt{b}(b + a)e^{jb} \int_{\sqrt{b}}^{\infty} \frac{e^{-j\tau^2}}{\tau^2 + a} d\tau \tag{24}$$

with $\arg(\sqrt{b}) \in (-3\pi/4, \pi/4)$. Its arguments in (22) are defined as

$$b_m = k\frac{rr'}{r + r'}[1 - \cos(\beta_m - \beta'_m)] \tag{25}$$

and

$$\begin{aligned} a_m^{\pm}(\Phi_m) = {} & k\frac{rr'}{r + r'} \sin\beta_m \sin\beta'_m \\ & \cdot \left[1 + \cos\left(\Phi_m - 2N_m^{\pm} n_m \pi\right)\right] \end{aligned} \tag{26}$$

where $N_m^{\pm}$ is the integer that nearest satisfies

$$\Phi_m - 2N_m^{\pm} n_m \pi = \pm\pi. \tag{27}$$

A simple algorithm for the numerical computation of (24) is suggested in [28]. The distance parameters defined in (26) are strictly related to the arguments of the UTD Fresnel transition functions of the wedge diffracted field $\Psi_m^{\mathrm{edge}}(P, P')$ defined in [1], and reduce to them on the SBC where $\beta'_m = \beta_m$. Note that, though the various contributions D_m^{tip} associated to the various edges do not depend on the tip angle (i.e., the angle between two consecutive edges), when they are summed in the total vertex diffraction coefficient D^{tip}, their combination is affected by the tip angle. For instance, if the tip angle between two edges in a plane angular sector approaches 180°, the two end-point contributions relevant to the two edges cancel, and the total vertex contribution vanishes, as expected.

III. Analysis of the Scalar Solution

In this section we analyze the behavior of the above obtained solution for the vertex diffracted field in (20), with special attention to the analytical description of its behavior in the transition regions, thus demonstrating its capability of restoring the total field continuity. It is well known that the GO shadow boundaries in the wedge problem have a planar shape. The incident shadow boundary plane (SBP) occurs at $\phi_m = \phi'_m \pm \pi$, whereas the SBPs relevant to the reflection from the faces $\phi_m = 0$ and $\phi_m = n_m\pi$ occur at $\phi_m = \pi - \phi'_m$ and $\phi_m = (2n_m - 1)\pi - \phi'_m$, respectively. The SBPs associated to two wedges delimiting a face of the pyramid intersect in a line passing through the vertex of the pyramid (arrows in Fig. 4(a)–(b)). When observing on this line two possible situations may happen. When the intersection is formed by the reflection SBPs, the reflection point lies exactly at the tip of the pyramid [Fig. 4(a)]. When instead the intersection is formed by the incident SBPs, the direct GO ray is intercepted by the tip [Fig. 4(b)]. Wedge diffracted contributions also have a shadow boundary because of the finiteness of the edges. Their shadow and the lit regions are separated by a shadow boundary cone (SBC), which represents the limit condition when the diffraction point on the edge lies at the tip of the pyramid; hence, the SBC coincides with the Keller diffraction cone when its tip is located exactly at the tip of the pyramid [Fig. 4(a)–(b)]. Therefore, the surface of the SBC associated to wedge m occurs at $\beta_m = \beta'_m$. It is important to note that the two SBCs associated to contiguous wedges, delimiting the same face of the pyramid, intersect at the same line where the two GO SBPs intersect [Fig. 4(a)–(b)]. Indeed, the GO and the two wedge diffracted fields may experience a discontinuity there, furthermore the two wedge diffracted fields are in transition there because they need to compensate for the GO discontinuity. At this peculiar observation aspect, the vertex diffracted field exhibits a *double* transition able to restore the continuity of the total field.

A. Far From Transition

When observing "far" from the SBCs the vertex diffracted field exhibits a ray optical behavior. We define "far" from the SBC, all spatial locations that are associated to the large parameter $b_m \gg 1$. This condition is encountered outside a transition region which envelopes the SBC and whose section in any plane containing the mth edge exhibits the typical parabolic shape of diffraction transition regions. Therefore, the angular extension of the transition region in terms of angular coordinates β_m becomes narrower for larger r, r', and eventually vanishes in the plane-wave far-field regime $r/\lambda, r'/\lambda \to \infty$ where the transition region collapse to the SBC. The latter case is of interest in RCS prediction. For $b_m \gg 1$, in (24)

$$\int_{\sqrt{b}}^{\infty} \frac{e^{-j\tau^2}}{\tau^2 + a} d\tau \sim \frac{e^{-jb}}{j2\sqrt{b}(b+a)} \tag{28}$$

so that the transition function in (21) and (22) $T_{\mathrm{GFI}} \to 1$, and the diffraction coefficient expression in (22) can be greatly simplified. Therefore, "far" from the SBCs the asymptotic order of the tip diffracted field is $\Psi^{\mathrm{tip}} = O(k^{-1})$, and the field attenuates strictly as $1/r$ away from the tip. In other words the field is a spherical wave arising from the tip of the pyramid.

B. In Transition Behavior

When approaching the SBC relative to wedge m, the m tagged term of vertex diffracted field in (20) exhibits a transition. Approaching this SBC, one has $\beta_m \to \beta'_m$, therefore the distance parameter defined in (25) $b_m \to 0$, the transition function reduces to

$$\lim_{b\to 0} T_{\mathrm{GFI}}(b, a) = \sqrt{j\pi b}\, F(a) \tag{29}$$

where $F(a)$ is the UTD Fresnel transition function [1]. Furthermore, when $\beta_m \to \beta'_m$, in (23) the Rubinowicz parameter $u_m \to 0$, and one has $B(\Phi, 0) = \cot[\Phi/(2n)]/(2n)$ in (22), which is equal to the UTD angular function reported in [1]. It is now easy to verify that when approaching the mth SBC ($\beta_m \approx \beta'_m$) the vertex diffracted field grows to the asymptotic order $\Psi_m^{\mathrm{tip}} = O(k^{-1/2})$ and assumes the value

$$\Psi_m^{\mathrm{tip}} \sim \frac{1}{2}\Psi_m^{\mathrm{edge}} \mathrm{sgn}(\beta_m - \beta'_m) + O(k^{-1}) \tag{30}$$

that allows to exactly compensate for the discontinuity of the mth wedge diffracted contribution $\Psi_m^{\mathrm{edge}} U(\beta'_m - \beta_m)$ in (17), across the mth SBC. At the SBC associated to the mth edge, i.e., when $\beta_m \approx \beta'_m$, it is possible to give a precise estimate of the field. The sum of the edge diffracted field and the mth term of the vertex diffracted field is continuous and equal to one half the diffracted field contribution plus higher order terms:

$$\Psi_m^{\mathrm{edge}} U(\beta'_m - \beta_m) + \Psi_m^{\mathrm{tip}} = \frac{1}{2}\Psi_m^{\mathrm{edge}} + O(k^{-1}). \tag{31}$$

C. Double Transition

As mentioned above, the SBCs relevant to a couple of contiguous wedges, say m and m +1, delimiting the face m of the pyramid, intersect in a semi-infinite line where also the two GO SBPs intersect. Approaching this particular aspect the GO contribution is discontinuous when crossing one of the SBPs and thus also when crossing the intersection line. However,

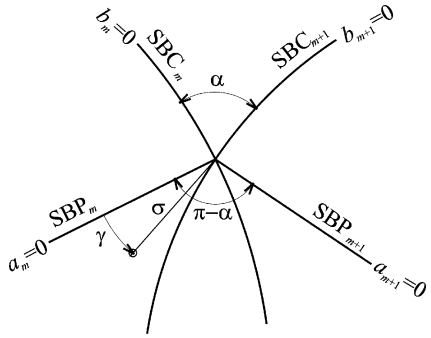

Fig. 5. Intersection of the two SBCs and the two SBPs. Parameterization of the observation aspect in the neighborhood of the double transition aspect for the computation of the vertex diffracted field behavior in that limit.

the wedge diffracted contributions $\Psi_m^{\rm edge}(P,P')U(\beta'_m-\beta_m)$ and $\Psi_{m+1}^{\rm edge}(P,P')U(\beta'_{m+1}-\beta_{m+1})$ from the two wedges are discontinuous, when the observation point P crosses the respective SBCs [Fig. 4(b)] or their intersection. Furthermore, near the SBC-SBP intersection the wedge diffracted fields $\Psi_m^{\rm edge}(P,P')$ and $\Psi_{m+1}^{\rm edge}(P,P')$ are in transition because the observation is close to the GO SBP, hence their asymptotic behavior is grown to the GO order $O(k^0)$, as described by the UTD Fresnel transition function with vanishing argument $a_m^{\pm}(\Phi_m)$ (see [1] for more details). Therefore, the job of the vertex contribution $\Psi^{\rm tip}(P,P')$ is to restore the continuity of the total field. In this limit both $\beta_m\approx\beta'_m$ and $\beta_{m+1}\approx\beta'_{m+1}$, thus $b_m\to 0$ and $b_{m+1}\to 0$; furthermore, for each wedge, one of the four UTD distance parameters (26) vanishes since approaching the associated SBP. We generically denote by $a_m\to 0$ and $a_{m+1}\to 0$ the vanishing parameter in (26), relevant to edges mth and $m+1$th.

It is interesting to note that the sum $b_p+a_p\,(p=m,m+1)$ is the difference of the optical lengths between the path of the vertex ray $P'OP$ (Fig. 1) and that of the GO ray (e.g., $P'P$ for the direct GO ray, or $P'Q_RP$ for the reflected GO ray, as shown in Fig. 2), and it is therefore the same when measured in the mth or in the $(m+1)$th edge reference system, as shown in (56); hence $a_m+b_m=a_{m+1}+b_{m+1}\to 0$. Hence, when approaching the double transition region (the intersection of the SBCs and the SBPs) the four distance parameters involved can be alternatively represented in terms of three independent parameters, as

$$\begin{cases} b_m=\sigma\cos^2\gamma \\ a_m=\sigma\sin^2\gamma \end{cases}\ \text{and}\ \begin{cases} b_{m+1}=\sigma\cos^2(\pi-\alpha-\gamma) \\ a_{m+1}=\sigma\sin^2(\pi-\alpha-\gamma) \end{cases} \tag{32}$$

with $\sigma\to 0$ approaching the double transition from the angular direction γ (Fig. 5). It is convenient to define as α the angle between the surfaces locally (at the intersection) tangent to the two SBCs. Since SBC_m and SBP_m are locally orthogonal, the angle between the SBPs is $\pi-\alpha$.

1) UTD Contributions (GO and Wedge Diffracted Fields): By using the introduced parameterization, with reference, for example, to the reflection case of Fig. 4, the lit and shadow regions of the field contributions $\Psi^{\rm GO}$, $\Psi_m^{\rm edge}$, and $\Psi_{m+1}^{\rm edge}$ are expressed in terms of the approaching angle γ (measured from the mth SBP, Fig. 5), regardless of the value of the parameter σ. The GO contribution vanishes in the range $\pi-\alpha<\gamma<2\pi$, whereas the field diffracted by the wedge m vanishes outside the SBC_m and exhibits a discontinuity across the SBP_m at $\gamma=0$; namely, near the intersection

$$\Psi_m^{\rm edge}\approx\begin{cases} -\frac{1}{2}\Psi^{\rm GO} & \text{for } 0<\gamma<\frac{\pi}{2} \\ 0 & \text{for } \frac{\pi}{2}<\gamma<\frac{3\pi}{2} \\ \frac{1}{2}\Psi^{\rm GO} & \text{for } \frac{3\pi}{2}<\gamma<2\pi. \end{cases} \tag{33}$$

Analogously the field diffracted by wedge $m+1$ vanishes outside the SBC_{m+1} and exhibits a discontinuity across the SBP_{m+1} at $\gamma=\pi-\alpha$; namely, near the intersection

$$\Psi_{m+1}^{\rm edge}\approx\begin{cases} 0 & \text{for } \gamma<\frac{\pi}{2}-\alpha \text{ and } \gamma>\frac{3\pi}{2}-\alpha \\ -\frac{1}{2}\Psi^{\rm GO} & \text{for } \frac{\pi}{2}-\alpha<\gamma<\pi-\alpha \\ \frac{1}{2}\Psi^{\rm GO} & \text{for } \pi-\alpha<\gamma<\frac{3\pi}{2}-\alpha. \end{cases} \tag{34}$$

As a matter of fact, the standard UTD field (i.e., the sum of the GO and the wedge diffraction contributions) is discontinuous at the SBCs. Therefore, at the intersection of the SBCs and SBPs, the asymptotic order of the discontinuity is $O(k^0)$, which is the asymptotic order of the GO field contribution. Indeed, the sum of the GO contribution and the $O(k^0)$ terms of the wedge diffracted contributions vanishes in the region internal or external to both the SBCs (terms of the order of $O(k^{-1/2})$ and higher do not vanish there), whereas it equals $\psi^{\rm GO}/2+O(k^{-1/2})$ in the region internal to a SBC but external to the other. In summary, the dominant asymptotic order $O(k^0)$ of the field near the intersection is shown in (35), at the bottom of the page.

2) Vertex Contribution: We explain now how the vertex diffracted field behaves and show that it restores the required continuity. As already noted for both edges m and $m+1$ a couple of parameters a,b vanish. Therefore we will use the limit

$$\lim_{b,a\to 0} T_{\rm GFI}(b,a)=2j\sqrt{\frac{b}{a}}(b+a)\tan^{-1}\left(\sqrt{\frac{a}{b}}\right) \tag{36}$$

(we have dropped the subscripts m and $m+1$) which will allow to determine the behavior of the vertex contributions relevant to the m and $m+1$ edges close to the double transition aspect. Considering the vertex diffracted field expressions (19)–(21) and using (36) in (22), one can see that the vertex diffracted field near the transition has the asymptotic order $\Psi_{m,m+1}^{\rm tip}\sim O(k^0)$. In other words, the order of the vertex diffracted field from $O(k^{-1})$, far from transition regions, grew to the asymptotic

$$\Psi^{\rm GO}+\Psi_m^{\rm edge}+\Psi_{m+1}^{\rm edge}\approx\begin{cases} 0 & \text{for } \frac{\pi}{2}-\alpha<\gamma<\frac{\pi}{2} \text{ and } \frac{3\pi}{2}-\alpha<\gamma<\frac{3\pi}{2} \\ \frac{1}{2}\Psi^{\rm GO} & \text{elsewhere.} \end{cases} \tag{35}$$

order of the GO contribution. After long but simple algebraic manipulation one can show that

$$\Psi_m^{\rm tip} \sim \frac{1}{2\pi}\Psi^{\rm GO}\tan^{-1}(\tan\gamma) = \begin{cases} \frac{1}{2\pi}\Psi^{\rm GO}\gamma & \text{for } 0<\gamma<\frac{\pi}{2} \\ \frac{1}{2\pi}\Psi^{\rm GO}(\gamma-\pi) & \text{for } \frac{\pi}{2}<\gamma<\frac{3\pi}{2} \\ \frac{1}{2\pi}\Psi^{\rm GO}(\gamma-2\pi) & \text{for } \frac{3\pi}{2}<\gamma<2\pi \end{cases} \quad (37)$$

and

$$\Psi_{m+1}^{\rm tip} \sim \frac{1}{2\pi}\Psi^{\rm GO}\tan^{-1}(\tan(\pi-\alpha-\gamma)) = \begin{cases} \frac{1}{2\pi}\Psi^{\rm GO}(-\alpha-\gamma) & \text{for } 0<\gamma<\frac{\pi}{2}-\alpha \\ \frac{1}{2\pi}\Psi^{\rm GO}(\pi-\alpha-\gamma) & \text{for } \frac{\pi}{2}-\alpha<\gamma<\frac{3\pi}{2}-\alpha \\ \frac{1}{2\pi}\Psi^{\rm GO}(2\pi-\alpha-\gamma) & \text{for } \frac{3\pi}{2}-\alpha<\gamma<2\pi \end{cases} \quad (38)$$

respectively. Since the $\tan^{-1}$ (inverse tangent function) in (36) is inverted in the range $-\pi/2 < \tan^{-1}x < \pi/2$, (37) and (38) are piecewise linear functions of the approaching angle γ, with a zero at the respective SBP and a jump discontinuity $\mp\psi^{\rm GO}/4$ at the respective SBC. Despite the value of each term in the vertex contribution depends on the approaching angle, and would resulting in a non physical behavior as highlighted in [25] with reference to the coefficient proposed in [18], the sum of the two m and $m+1$ terms, and in turn the entire vertex contribution, exhibits a behavior independent of γ except for a discontinuity at the SBCs, i.e., (39), shown at the bottom of the page. Thus, without affecting the GO-discontinuity compensation by the transition behavior of the UTD contributions at SBPs, the vertex contribution compensates for the discontinuities of UTD wedge contributions at the SBCs providing a continuous total field value that is independent of the approaching angle γ, as required for a physically sound solution. The limit value of the leading asymptotic term $O(k^0)$ of total field at the double transition aspect is

$$\Psi^{\rm tot} \sim \Psi^{\rm GO} + \Psi_m^{\rm edge} + \Psi_{m+1}^{\rm edge} + \Psi_m^{\rm tip} + \Psi_{m+1}^{\rm tip} \sim \frac{\pi-\alpha}{2\pi}\Psi^{\rm GO}. \quad (40)$$

Equation (40) is interpreted as follows. When the reflection point (Fig. 2) coincides exactly with the vertex, the GO applied to the reflected ray tube would predict a lit region in a sector below the SBPs (of subtended angle $\pi-\alpha$) and a shadowed region above the SBPs (of subtended angle $\pi+\alpha$), as shown in Fig. 4. Hence, the field associated to the ray is a percentage of the GO reflected field that is proportional to the width of the lit area in the tube section, namely the ratio $(\pi-\alpha)/(2\pi)$. This result coincides with the asymptotic evaluation of the radiation integral using the Physical Optics approximation (not shown here), which provides a correct result to the asymptotic order k^0.

IV. The Cases of Plane Wave Incidence and Far Field Observation

The solution presented in (20)–(26) is valid for source and observation at a finite distance from the vertex. Here we provide the expressions for the particular cases: (a) plane wave incidence and observer at finite distance; (b) source at finite distance and far field observation; and (c) plane wave incidence and far field observation (the RCS case). For unitary plane wave incidence, the final expressions are derived by multiplying (20) by $4\pi r'/e^{-jkr'}$ and by letting $r'\to\infty$ in (20)–(26). Accordingly, an incident plane wave with value $\Psi^{\rm inc}(O)$ at the tip location O produces a vertex diffracted field at P given by (20) where $\Psi^{\rm inc}(O)$ replaces $\Psi^{\rm inc}(O,P')$. The diffraction coefficients $D^{\rm tip}$ and $D_m^{\rm tip}$ in (19)–(21) are still based on the same expression (22). Furthermore, the limit $r'\to\infty$ implies that $rr'/(r+r')\to r$, and thus the arguments (26) and (25) of the GFI Transition functions $T_{\rm GFI}$ in (22), become

$$b_m = kr[1-\cos(\beta_m-\beta_m')] \quad (41)$$

and

$$a_m^{\pm}(\Phi_m) = kr\sin\beta_m\sin\beta_m'[1+\cos(\Phi_m-2N_m^{\pm}n_m\pi)]. \quad (42)$$

Here, β_m' and ϕ_m' represent the plane wave incidence angles in the reference system associated to the mth edge (Figs. 1 and 4). The same discussion carried out in Section III about the transition regions and limits still applies to this particular case.

For the case with source at finite distance and observer in the far field, we multiply (20) by re^{jkr} and let $r\to\infty$. Therefore the far field diffracted field is given by (20) with the last spherical spreading factor suppressed and implicitly intended in the far field normalization. Furthermore, the far field assumption in (26) and (25) implies that $rr'/(r+r')\to r'$, and thus the TGF parameters to be used in (22) are as in (41) and (42) once r has been replaced by r'.

Finally, in the RCS case, i.e., for plane wave incidence and far field observation, as pointed out in Section III.A, the GFI Transition functions $T_{\rm GFI}$ in (22) become unity. In this case the vertex contribution in (22) is correctly singular on the SBCs (i.e., when $\beta_m\to\beta_m'$). However, when modeling a finite structure like the polygonal plate in Fig. 6, the scattered field is only represented by the sum of the tip contributions $\Psi^{{\rm tip},i}$ associated to its vertexes $\mathbf{v}_i, i=1,\ldots,N$

$$\Psi^{\rm tot} = \sum_{i=1}^{N}\Psi^{{\rm tip},i} = \sum_{i=1}^{N} e^{-jk(\hat{\mathbf{r}}'-\hat{\mathbf{r}})\cdot\mathbf{v}_i}\sum_{m=1}^{M_i} D_m^{{\rm tip},i} \quad (43)$$

with M_i denoting the number of edges intersecting at $\mathbf{v}_i$ (a flat plate has $M_i=2$, for $i=1,\ldots,N$). We denote by $\mathbf{l}_i = \mathbf{v}_{i+1}-\mathbf{v}_i$ (assume $\mathbf{v}_{N+1}\equiv\mathbf{v}_1$ for convenience) the polygonal plate sides, and we assume for convenience that at $\mathbf{v}_{i+1}$ $m=1$ tags the contribution associated to the previous edge $\mathbf{l}_i$, whereas $m=2$ tags the contribution associated to the following edge

$$\Psi^{\rm tip} \sim \Psi_m^{\rm tip} + \Psi_{m+1}^{\rm tip} \sim \begin{cases} \frac{\pi-\alpha}{2\pi}\Psi^{\rm GO} & \text{for } \frac{\pi}{2}-\alpha<\gamma<\frac{\pi}{2} \text{ and } \frac{3\pi}{2}-\alpha<\gamma<\frac{3\pi}{2} \\ -\frac{\alpha}{2\pi}\Psi^{\rm GO} & \text{elsewhere.} \end{cases} \quad (39)$$

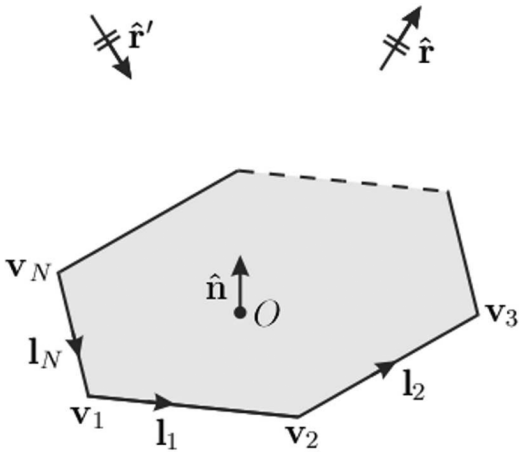

Fig. 6. Geometry of a polygonal plate with N vertexes for the RCS case.

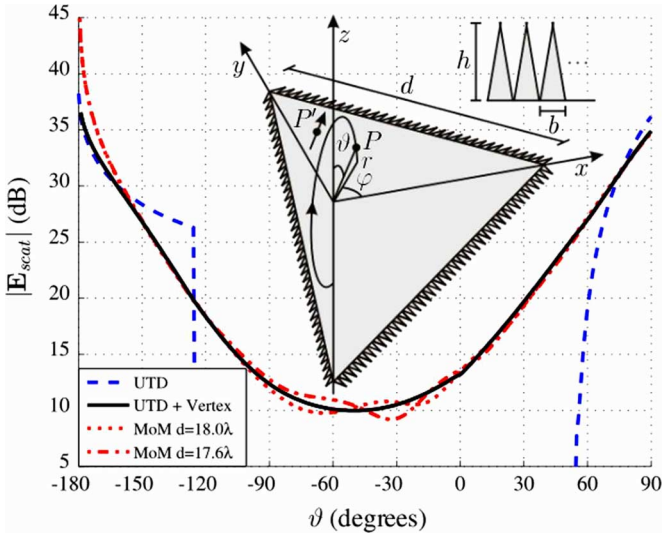

Fig. 7. Amplitude of the field scattered by an orthogonal pyramid illuminated by an electric dipole at P' on a circular scan from one edge to the opposite face (see the inset). Standard UTD solution (dashed line), UTD plus vertex contribution (continuous line), MoM solution for $d = 18\lambda$ (the dotted line) and $d = 17.6\lambda$ (dash-dotted line).

$\mathbf{l}_{i+1}$. The two tip contributions $D_2^{\mathrm{tip},i}$ and $D_1^{\mathrm{tip},i+1}$, at $\mathbf{v}_i$ and $\mathbf{v}_{i+1}$, respectively, both relevant to the same finite edge $\mathbf{l}_i$, have the same SBC angle where they cancel each others' singularity, so that the total field is uniform. Also, in the forward or reflection direction of the polygonal plate, where all the SBCs of all the edges intersect, all the individual vertex contributions are singular but their sum is uniform and exactly recovers the PO prediction

$$\Psi^{\mathrm{tot}} = \mp\frac{jkA}{2\pi}\hat{\mathbf{r}}'\cdot\hat{\mathbf{n}} + O(k^0) \tag{44}$$

in which the plus sign applies to the forward direction observation and to the reflection direction observation for *soft* boundary conditions on A, whereas the minus sign applies to the reflection direction observation for *hard* boundary conditions on A. A proof for (44) is given in Appendix B in connection with the limit of Gordon's formula for the same forward/reflection directions, fully exploited in [36]. In fact, Rubinowicz's theory, which our formulation is based on, can be formulated also under the Kirchhoff-Helmholtz (PO) approximation [32], and reduces to Gordon's formulation as a special case in the plane-wave far-field regime.

V. Electromagnetic Case

The solution for the scalar case is here directly employed to build the solution for the electromagnetic diffraction at a perfectly conducting pyramid illuminated by an arbitrarily polarized electromagnetic spherical or plane wave. In this section we present a ray description in the UTD standard format, leading to a dyadic compact expression for the vertex diffraction coefficient. On each mth edge we define a *ray-fixed* [1] spherical reference system with origin at the pyramid vertex; the incidence unit vectors are denoted by $(-\hat{\mathbf{r}}', \hat{\boldsymbol{\beta}}_m', \hat{\boldsymbol{\phi}}_m')$ and the observation unit vectors by $(\hat{\mathbf{r}}, \hat{\boldsymbol{\beta}}_m, \hat{\boldsymbol{\phi}}_m)$. This allows to express the arbitrarily polarized electric field incident at the tip in either of the M edge reference systems as $\mathbf{E}^i(O) \equiv E^i_{\beta'_m}\hat{\boldsymbol{\beta}}_m' + E^i_{\phi'_m}\hat{\boldsymbol{\phi}}_m'$ and the vertex diffracted field as $\mathbf{E}^{\mathrm{tip}}(P,P') \equiv \boldsymbol{E}^{\mathrm{tip}}_{\beta_m}\hat{\boldsymbol{\beta}}_m + \boldsymbol{E}^{\mathrm{tip}}_{\phi_m}\hat{\boldsymbol{\phi}}_m$. The diffracted field is thus expressed in a compact way as

$$\mathbf{E}^{\mathrm{tip}}(P,P') = \mathbf{E}^i(O)\cdot\underline{\underline{\mathbf{D}}}^{\mathrm{tip}}\frac{e^{-jkr}}{r} \tag{45}$$

with the dyadic vertex diffraction coefficient is given by

$$\underline{\underline{\mathbf{D}}}^{\mathrm{tip}} = \sum_{m=1}^{M}\left(-\hat{\boldsymbol{\beta}}'_m\hat{\boldsymbol{\beta}}_m\boldsymbol{D}_m^{\mathrm{tip},s} - \hat{\boldsymbol{\phi}}'_m\hat{\boldsymbol{\phi}}_m\boldsymbol{D}_m^{\mathrm{tip},h}\right) \tag{46}$$

in which $D^{\mathrm{tip},s}$ and $D^{\mathrm{tip},h}$ are the scalar diffraction coefficients derived in the previous section for *soft* (s) or *hard* (h) boundary condition, i.e., by choosing the upper or lower sign in (22), respectively.

The analysis of the electromagnetic solution is very similar to that of scalar one presented in Section III and leads to the same conclusions. We omit it for brevity and present instead, in the next section, some numerical examples of application of the electromagnetic case also comparing the results against those provided by the Method of Moments (MoM).

VI. Numerical Results

To analyze the behavior of the field scattered by a single pyramid vertex, let us consider first a perfectly conducting orthogonal pyramid formed by three orthogonal edges; this is a very common configuration present at any vertex in any cube or parallelepiped. The three edges coincide with the $x > 0, y > 0$ and $z < 0$ semiaxes of a Cartesian reference system with origin at the tip, as shown in the inset of Fig. 7. In the ray analysis the pyramid is assumed as infinite, and thus each face is an infinite quarterplane. The scattering case considered is chosen to verify the various transitional behavior of the diffraction coefficient, as discussed in Section III. The results are validated against those

from a MoM, and in this numerical analysis the perfectly conducting faces of the pyramid have to be truncated; each face is thus an electrically large triangle with basis d (see insets of Fig. 7). Such truncations introduce perturbations that, in a ray picture, are associated to further diffraction mechanisms, like additional edge and vertex diffractions at the bases of the triangular plates, that are not negligible especially in deep shadow regions. To isolate and better describe the effect of diffraction at a single vertex we do not want to include further diffraction contributions in our ray analysis. Therefore, besides having source and observer close to the considered vertex, in order to reduce the effects of the plates truncations in the MoM solution, we added to the bases of the plates a "fence" of small perfectly conducting triangles whose bases and heights are $b = 0.1\lambda$ and $h = 0.25\lambda$, respectively. The observation point P moves along a circular scan of radius $r = 1.3\lambda$, with $\varphi = 45°$ (symmetric with respect to the pyramid top face) and $-180° < \vartheta < 90°$. The pyramid is illuminated by a unitary momentum $I\Delta\ell = 1$ Am electric dipole placed at $P' = (-1, -1, 1)\lambda$ and directed along the unit vector $\hat{p} = 0.5(1, 1, \sqrt{2})$. Along the considered scan, two distinct compensation mechanisms (transition regions) occur. At $\vartheta \approx -125°$ the observation point crosses the SBC associated to the edge on the z axis. Here the wedge diffracted ray contribution, which is present in the range $-180° \leq \vartheta \leq -125°$, abruptly disappears, while the vertex diffracted ray contribution experiences a transition as described in Section III.B. At $\vartheta \approx 54°$ a different transition occurs: there the observation point is at the intersection of the two reflection SBPs and two SBCs, associated to the edges along the x and y axes [see Fig. 4(a)], where the vertex contribution experiences the double transition described in Section III.C and must compensate for the simultaneous appearance of the reflected GO ray and of the two wedge diffracted rays arising from the edges along x and y axes. The amplitude of the scattered field along the scan is shown in Fig. 7. The dashed line refers to the standard UTD solution, which consists of the GO reflected field and the singly edge-diffracted fields. This solution is discontinuous at $\vartheta \approx -125°$ where a the wedge diffracted field contribution from the edge along the z-axis disappears, it vanishes in the range $-125° \leq \vartheta \leq 54°$ where a zero field is predicted by the UTD, and exhibits a cusp (discontinuity in the derivative) at $\vartheta \approx 54°$, at the simultaneous appearance of the GO and of the two in-transition wedge diffracted rays, as detailed in Section III.C. In the case considered the direct GO contribution never disappears, therefore the wedge diffracted fields do not need to be discontinuous to compensate for the direct GO disappearance. Therefore, to emphasize the compensation mechanisms we plot the scattered field, instead of the total field. The continuous line (UTD+Vertex) refers to the UTD solution augmented by our vertex contribution (45), that smoothly compensates for the standard UTD discontinuity and cusp, at the two different kind of SBs described above. Note that besides rendering the field continuous, our UTD+Vertex field evaluation is also in good agreement with the MoM solution (dot and dash-dot curves). To emphasize that the small difference between our UTD+Vertex and MoM solutions arises from the truncation of the plates, we consider two MoM solutions relative to plates with different base measures; the dotted line refers to $d = 18\lambda$, while the dash-dotted line refers to $d = 17.6\lambda$. As expected, when observing close to the edges (for $\vartheta = -180°$ in Fig. 7), the UTD reproduces a weaker field singularity than that in the MoM which accounts also for the near field effects. However, when P approaches a pyramid face ($\vartheta = 90°$ in Fig. 7), the agreement is very good. The truncation effects are clearly visible in the weak field region of the scan where, for the infinite structure, only the vertex contribution is present. In this weak field region, truncation effects, present only in the MoM solution, interfere with the vertex ray-field creating ripples whose maxima and minima changes for different truncation size. It is important to note that the difference between the two MoM solutions (relative to two different truncations) is of the same order of the difference between the MoM results and our UTD+Vertex solution.

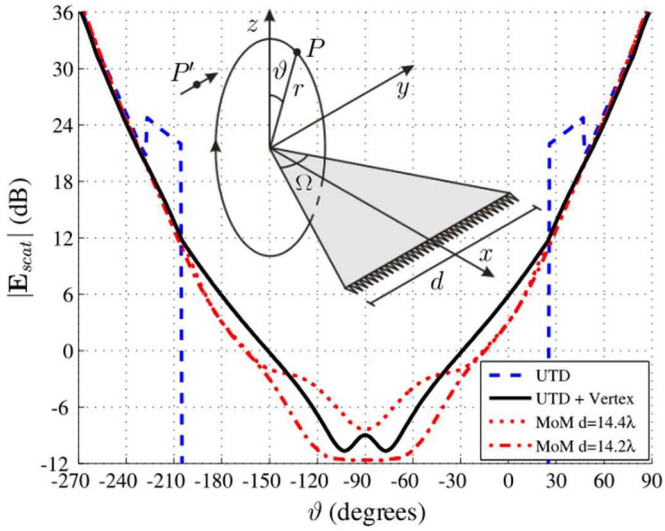

Fig. 8. Amplitude of field scattered by a $\Omega = 30°$ plane angular sector, illuminated by an electric dipole at P', on a circular scan orthogonal to the sector plane (see the inset). Standard UTD solution (dashed line), UTD plus vertex contribution (continuous line), MoM solution for $d = 14.4\lambda$ (the dotted line) and $d = 14.2\lambda$ (dash-dotted line).

In the second example analyzed in this paper, we still focus on the properties of vertex diffraction at a single vertex, considering a perfectly conducting plate with infinite extent. The plane angular sector is in the xy plane and has its edges along the $\hat{x}\cos(\Omega/2) \pm \hat{y}\sin(\Omega/2)$ directions, as shown in Fig. 8; the tip angle is $\Omega = 30°$. The plane angular sector is illuminated by a unitary momentum electric dipole $I\Delta\ell = 1$ Am at $P' = (-1, -1, 1)\lambda$, oriented along $\hat{p} = (0, 1, 0)$. The observation point P scans a circle of radius $r = 1.3\lambda$ in the xz plane (Fig. 8). Also in this case, in order to reduce the truncation effects, we added a fence of small triangles $(b = 0.1\lambda, h = 0.25\lambda)$ to the triangular plate in the MoM model. In Fig. 8 the amplitude of the scattered field along the scan is shown. Similarly to the previous examples, the standard UTD solution (dashed line) exhibits jump discontinuities at $\vartheta \approx -227°, 47°$ and at $\vartheta \approx -205°, 25°$ when crossing the two SBCs associated to the two edges, respectively, and vanishes for $-205° \leq \vartheta \leq 25°$, i.e., inside both the SBCs. The introduction of the vertex contribution smoothly compensates for these discontinuities providing a continuous total field (continuous line). Despite the

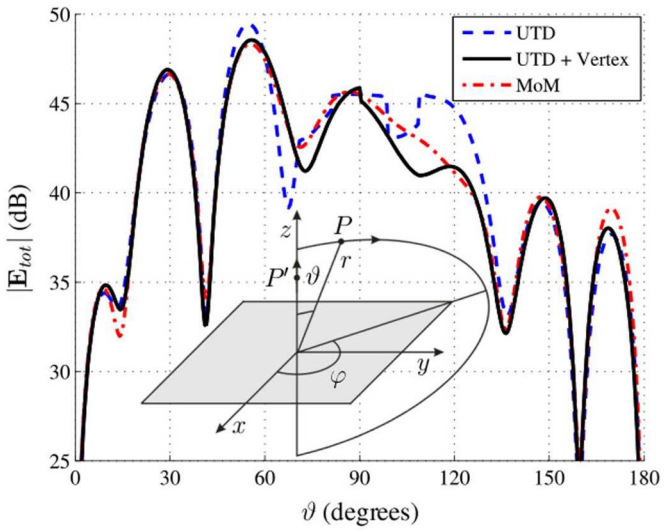

Fig. 9. Amplitude of the total far field radiated by an electric dipole placed over a $4\lambda \times 4\lambda$ square perfectly conducting plate. Standard UTD solution (dashed line), UTD plus vertex contribution (continuous line), MoM (dash-dotted line).

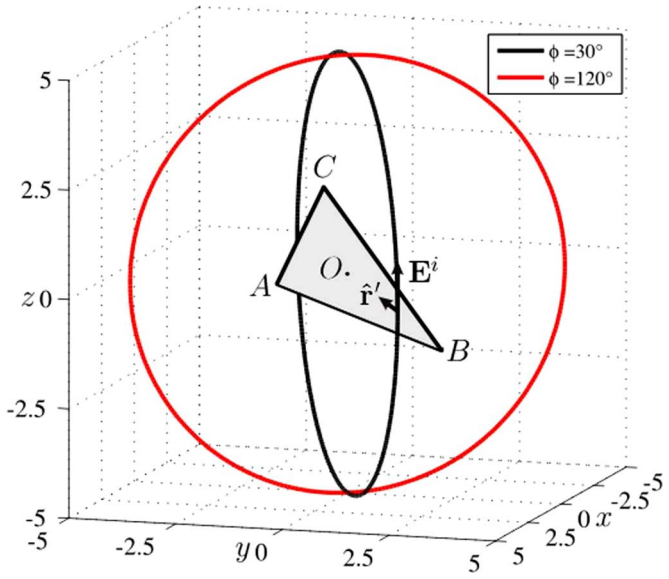

Fig. 10. Triangular plate geometry and bistatic RCS arrangement: illumination from $(\vartheta', \varphi') = (90°, 30°)$ with vertical polarization, observation along the two scan plane at $\varphi = 30°$ (inner oblong circle) and $\varphi = 120°$ (outer circle).

sharp tip angle, after the introduction of our first-order vertex diffraction coefficient, which does not accounts for multiple wedge interaction effects, the UTD+Vertex solution is in good agreement with the reference MoM solutions calculated for two different triangular plate sizes, i.e., $d = 14.4\lambda$ (dotted line) and $d = 14.2\lambda$ (dash-dotted line). Again, small truncation effects are visible in the MoM results in the weak field region around $\vartheta = -90°$.

Next, we consider a $4\lambda \times 4\lambda$ perfectly conducting square plate illuminated by a vertically oriented electric dipole, placed at $P' = (0, 0, 1)\lambda$ and unitary momentum. This case represents a more complex scenario that often occurs in the antenna radiation analysis, and requires the tracing and the description of four-edge and four-vertex rays. The total far field amplitude at a distance $r = 2D^2/\lambda$ (where D is diagonal of the square plate) for $\varphi = 135°$ and $0° < \vartheta < 180°$ is shown in Fig. 9. In this case, the standard UTD solution (dashed line) exhibits various discontinuities that are smoothed out by the introduction of the vertex contribution (continuous line). The residual discontinuity at grazing $\vartheta = 90°$ can be removed by introducing higher order contributions, like doubly diffracted rays [3], [5] that would also improve the UTD accuracy. Indeed, the agreement with the MoM solution is good except around grazing.

Finally, we analyze a bistatic RCS case. We consider a triangular plate with sides $\overline{AB} = 4\lambda, \overline{BC} = 5\lambda$, and $\overline{CA} = 3\lambda$ (Fig. 10). The triangular plate is tilted with respect to the xy plane; namely, the plate normal unit vector is pointed toward the spherical coordinates $\vartheta = 45°$ and $\varphi = 30°$, so that when a vertically polarized ($\mathbf{E}^i = E^i\hat{\mathbf{z}}$) plane wave impinges on the plate from $\vartheta' = 90°$ and $\varphi' = 30°$, it is reflected in the $\vartheta = 0°$ (positive z-axis) direction. The RCS is observed along two scan planes for $\varphi = 30°$ (inner oblong circle) and $\varphi = 120°$ (outer circle), respectively. The first observation scan cuts both the reflected and the forward scattering beams at $\vartheta = 0$ and $\vartheta = -90°$, respectively. The second scan cuts the reflected RCS beam at $\vartheta = 0°$ orthogonally to the first scan. As illustrated in Section IV, the Vertex RCS prediction (continuous line) recover that from PO both in the reflection and in the forward directions. Note also that results for the two scans agrees at scan intersection $\vartheta = 0°$, i.e., in the reflection direction, independently of the scan plane. This confirms that our Vertex contribution overcomes the problem highlighted in [25] about the formulation in [18]. The comparison with the MoM RCS results (dashed lines) shows how the Vertex results, which possess the correct wedge boundary conditions and φ-angular diffraction pattern, are more accurate than PO at those aspects dominated by single edge diffraction effects (e.g., $\varphi = 30°$ scan, grazing observation aspect $\vartheta = -45°$). The discrepancy between Vertex and MoM results for lower RCS levels is explained by the fact that minor lobes are due to higher order interaction (edge-vertex, vertex-edge, etc.) not accounted for in our first order model [37].

VII. Conclusion

In this paper we have presented a novel UTD diffraction coefficient for the ray diffracted at the tip of a pyramid, which can be used in the framework of the UTD (i.e., the sum of the GO and edge diffracted fields). The proposed vertex field expression has to be summed to the UTD field contributions thus providing an improved field accuracy, as we have shown analytically and in the numerical examples.

The solution is accurate because uniformly describes the proper transitional behavior of the vertex diffracted ray in connection with GO and UTD wedge ray discontinuities, thus providing a smooth total field. Furthermore the solution is very general because it can be applied to many different geometries like tip of pyramids, vertexes in plates and vertexes at the connection of various plates, also in open structures, as required for the high frequency analysis of general structures and scenarios.

We mention that closed form analytical solutions for the wedge and vertex diffracted field have been provided also in the time domain (TD) for short-pulse excitation. In particular, a

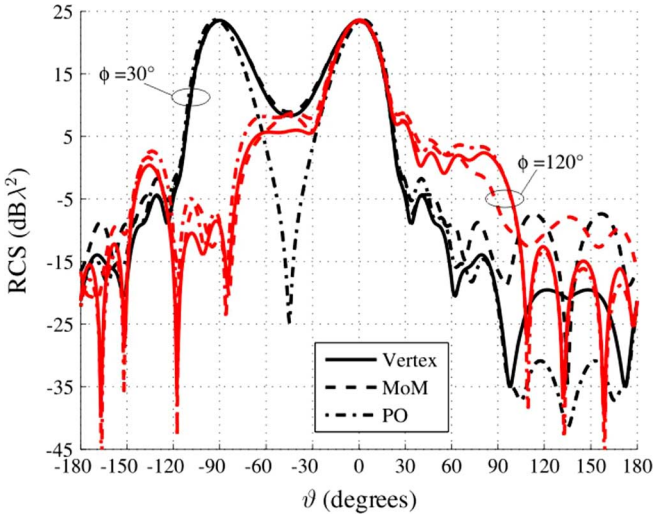

Fig. 11. Bistatic RCS for the triangular plate in Fig. 10 on the two scan planes $\varphi = 30°$ and $\varphi = 120°$. Vertex (continuous line), MoM (dashed line), and PO (dash-dotted line).

detailed transient analysis for the edge diffracted field was provided in [38], [39] allowing the development of a time domain version of the UTD [40]. The TD-UTD solution has been augmented by uniform expressions for TD doubly diffracted rays in [41]. The time domain version of the ITD has been presented in [42]. Based on that, a time domain closed form solution for vertex diffraction has been derived and summarized in [43].

Appendix A

In this Appendix the uniform asymptotic evaluation of (15) and (16) is carried out leading to (17) with the vertex field expression in (20). By using (9), (15) and (16) are decomposed as the sum of four terms each given by

$$I^{\mathrm{UTD}} = \int_{-\infty}^{\infty} 2B(\Phi_p, u(z_Q)) \frac{e^{-jkr_{PQ}}}{4\pi r_{PQ}} \frac{e^{-jkr_{P'Q}}}{4\pi r_{P'Q}} dz_Q \tag{47}$$

and

$$I^{\mathrm{tip}} = \int_{0}^{-\mathrm{sgn}(z_s)\infty} 2B(\Phi_p, u(z_Q)) \frac{e^{-jkr_{PQ}}}{4\pi r_{PQ}} \frac{e^{-jkr_{P'Q}}}{4\pi r_{P'Q}} dz_Q \tag{48}$$

respectively, with $\Phi_p = \pi \pm (\phi \pm \phi')$, and where we have dropped the subscript m for simplicity. The integrand of (47) and (48) exhibits a stationary phase point at $z_s = (\rho z' + \rho' z)/(\rho + \rho')$ [see (13)]. Furthermore it is singular at the pairs of complex conjugate poles

$$z_p = \Big[\rho^2 z' + \rho'^2 z + (z + z')\rho\rho' \cosh u_p \pm j\rho\rho' \sinh u_p \sqrt{\rho^2 + \rho'^2 + 2\rho\rho' \cosh u_p + |z - z'|^2}\Big] \cdot \left[\rho^2 + \rho'^2 + 2\rho\rho' \cosh u_p\right]^{-1} \tag{49}$$

with $u_p = \Phi_p - 2\pi nN$, and $N = 0, \pm 1, \pm 2 \cdots$. Note that the poles z_p may approach the real axis only at the stationary phase point, i.e., when $u_p \to 0$ (i.e., when the observer is at the SBP) one has that $z_p \to z_s$. Introducing in (47) and in (48) the change of variable $u = u(z_Q)$ defined by (11) (see also [31]), for which $r_{PQ} r_{P'Q} du = (r_{PQ} + r_{P'Q}) dz_Q$, leads to

$$I^{\mathrm{UTD}} = \frac{1}{2\pi} \int_{-\infty}^{\infty} B(\Phi_p, u) \frac{e^{-jkR(u)}}{4\pi R(u)} du \tag{50}$$

and

$$I^{\mathrm{tip}} = \frac{1}{2\pi} \int_{|u_m|}^{\infty} B(\Phi_p, u) \frac{e^{-jkR(u)}}{4\pi R(u)} du \tag{51}$$

respectively, with $R(u) = \sqrt{\rho^2 + \rho'^2 + 2\rho\rho' \cosh u + |z - z'|^2}$ and $u_m = u(z_s = 0)$ is the "Rubinowicz parameter" defined in (23).

Note that (50) is exactly one of the four terms constituting the wedge diffracted field [1]; its leading uniform asymptotic contribution, associated to the stationary phase point $u_s = 0$ can be evaluated as in [1] providing one of the four cotangent constituting the UTD wedge diffracted field $\Psi_m^{\mathrm{UTD}}(P, P')$ associated to edge m; the transition between the nearest poles and the stationary phase point $u_s = 0$ is managed by the UTD Fresnel transition function [1].

We stress again that in (51) the stationary phase point at $u_s = 0$ does not lie on the integration path (it lies in the missing part of the integration domain $(-\infty, |u_m|)$). Therefore, the leading asymptotic contribution of (51), associated to the end-point, is evaluated as follows. First, the change of variable $\tau^2 = k[R(u) - R(0)]$ is introduced for which $2\tau d\tau = k\partial R(u)/(\partial u) du$; next, the singularities of the integrand nearest to the saddle point $\tau = 0$ are described using an *ad hoc* regularizing function, i.e., by multiplying and dividing by $\tau^2 + k[R(0) - R(u_p)]$; finally, the slowly varying part of the integrand is evaluated at the end point and carried out of the integral. This procedure leads to

$$I^{\mathrm{tip}} = \frac{B(\Phi_p, u_m)}{2\pi jk \left.\frac{\partial}{\partial u} R(u)\right|_{u_m}} \frac{e^{-jkR(u_m)}}{4\pi R(u_m)} \cdot 2j\sqrt{k[R(u_m) - R(0)]}\, k[R(u_m) - R(u_p)] \cdot e^{jk[R(u_m) - R(0)]} \int_{\sqrt{k[R(u_m) - R(0)}}^{\infty} \frac{e^{-\tau^2}}{\tau^2 + k[R(0) - R(u_p)]} d\tau. \tag{52}$$

Denoting by

$$b_m = k[R(u_m) - R(0)] \tag{53}$$

the difference in electrical length between the vertex diffracted ray path $R(u_m)$ and the mth wedge diffracted ray path $R(0)$; and by

$$a_m^{\pm}(\phi_m \pm \phi'_m) = k[R(0) - R(u_p)] \tag{54}$$

the difference in electrical length between the mth wedge diffracted ray path $R(0)$ and the GO direct or reflected ray path $R(u_p)$, (52) reduces to

$$I^{\text{tip}} = \frac{B(\Phi_p, u_m)}{2jk\pi(\cos\beta'_m - \cos\beta_m)} \frac{e^{-jkr'}}{4\pi r'} \frac{e^{-jkr}}{r} \\ cdot T_{\text{GFI}}(b_m, a_m^{\pm}(\phi_m \pm \phi'_m)) \quad (55)$$

where the T_{GFI} function is defined in (24).

It is important to note that

$$b_m + a_m^{\pm}(\phi_m \pm \phi'_m) = k[R(u_m) - R(u_p)] \quad (56)$$

is the difference between the path length of the vertex diffracted ray and the path length of the GO ray, which is the same for all the edges; therefore $b + a$ is actually independent of the index m tagging the edges but it depends only on which GO ray is considered.

The distance parameters in (25) and (26) are approximations of those defined in (53) and (54), respectively, accordingly to the analogous simplification used in the UTD [1]. The approximation simplifies the calculation of the distance parameters (25) and (26) which can be expressed easily only in terms of the local vertex ray geometry, as required by the UTD scheme, and no longer involves information about the edge diffracted rays. Nonetheless, (25) and (26) recover the exact parameters (53) and (54) in the neighborhood of the aspects where they vanish, i.e., inside the transition region where the transition function T_{GFI} differs significantly from unity and describes the transitional behavior of the ray. Far from transition, where the parameters in (25) and (26) do not well approximate the exact ones (53) and (54), the T_{GFI} equals unity and therefore the non accurate approximation does not affect the result. Because of the approximation introduced, the property described in (56) does not hold rigorously for (25) and (26) but only in the limit $a_m, b_m \to 0$ for vanishing parameters, i.e., in the double transition.

Finally, all the analogous terms (55) are summed up and cast in the UTD format (20); those relevant to the mth wedge lead to the four terms in (22), contributions from all the edges are in turn summed in (21).

APPENDIX B

In this Appendix it is proved that, in the reflection and forward aspects, the RCS provided by the proposed tip diffraction coefficient for a polygonal plate equals that provided by PO. The scalar far field scattered in the direction $\hat{\mathbf{r}}$ by the polygonal plate in Fig. 6, when illuminated by a plane wave travelling along $\hat{\mathbf{r}}'$, is given by (43). When observing in the *forward direction* $\hat{\mathbf{r}} = \hat{\mathbf{r}}'$, in (43) each term $D_m^{\text{tip},i}$, with $m = 1, 2$ (see Section IV for symbol definitions), exhibits a double singularity. Indeed in the forward direction $\beta_m = \beta'_m$ and $\phi_m = \phi'_m \pm \pi$ so that in (22)

$$\frac{1}{\cos\beta'_m - \cos\beta_m} = \frac{1}{(\hat{\mathbf{r}}' - \hat{\mathbf{r}}) \cdot \hat{\mathbf{l}}_{i+2-m}} \to \infty \quad (57)$$

and

$$B(\pi \pm (\phi_m - \phi'_m), u_m) \approx \frac{(-1)^m}{2} \frac{(\hat{\mathbf{r}}' \times \hat{\mathbf{r}}) \cdot \hat{\mathbf{l}}_{i+2-m}}{1 - \hat{\mathbf{r}}' \cdot \hat{\mathbf{r}}} \to \infty \quad (58)$$

as can be easily derived by a small argument approximation of trigonometric and hyperbolic functions in (10). By using (57) and (58) in (22), the singular behavior at the forward observation aspect is calculated as

$$-D_2^{\text{tip},i+1} \approx D_1^{\text{tip},i} \approx \frac{1}{4jk\pi(\hat{\mathbf{r}}' - \hat{\mathbf{r}}) \cdot \hat{\mathbf{l}}_i} \frac{(\hat{\mathbf{r}}' \times \hat{\mathbf{r}}) \cdot \hat{\mathbf{l}}_i}{1 - \hat{\mathbf{r}}' \cdot \hat{\mathbf{r}}} \quad (59)$$

which is used in (43) leading to

$$\Psi^{\text{tot}} \approx -\sum_{i=1}^{N} \frac{e^{-jk(\hat{\mathbf{r}}' - \hat{\mathbf{r}}) \cdot \mathbf{v}_{i+1}} - e^{-jk(\hat{\mathbf{r}}' - \hat{\mathbf{r}}) \cdot \mathbf{v}_i}}{4jk\pi(\hat{\mathbf{r}}' - \hat{\mathbf{r}}) \cdot \hat{\mathbf{l}}_i} \frac{(\hat{\mathbf{r}}' \times \hat{\mathbf{r}}) \cdot \hat{\mathbf{l}}_i}{1 - \hat{\mathbf{r}}' \cdot \hat{\mathbf{r}}}. \quad (60)$$

Though each term is singular, the summation is not, as shown in the following. Each ith term of (60) can be rewritten as an integral along the ith side of the polygonal via the relation

$$\frac{e^{-jk(\hat{\mathbf{r}}' - \hat{\mathbf{r}}) \cdot \mathbf{v}_{i+1}} - e^{-jk(\hat{\mathbf{r}}' - \hat{\mathbf{r}}) \cdot \mathbf{v}_i}}{jk(\hat{\mathbf{r}}' - \hat{\mathbf{r}}) \cdot \hat{\mathbf{l}}_i} \\ = -e^{-jk(\hat{\mathbf{r}}' - \hat{\mathbf{r}}) \cdot \mathbf{v}_i} \int_0^{l_i} e^{-jk(\hat{\mathbf{r}}' - \hat{\mathbf{r}}) \cdot \hat{\mathbf{l}}_i l} dl \quad (61)$$

so that the summation in (60) reduce to an integral around the polygon perimeter C

$$\Psi^{\text{tot}} \approx \frac{1}{4\pi} \frac{\hat{\mathbf{r}}' \times \hat{\mathbf{r}}}{1 - \hat{\mathbf{r}}' \cdot \hat{\mathbf{r}}} \cdot \oint_C e^{-jk(\hat{\mathbf{r}}' - \hat{\mathbf{r}}) \cdot \mathbf{v}} d\mathbf{v}. \quad (62)$$

Finally, by invoking Stokes's theorem and

$$\nabla_{\mathbf{v}} \times \left[\frac{\hat{\mathbf{r}}' \times \hat{\mathbf{r}}}{1 - \hat{\mathbf{r}}' \cdot \hat{\mathbf{r}}} e^{-jk(\hat{\mathbf{r}}' - \hat{\mathbf{r}}) \cdot \mathbf{v}} \right] = jk(\hat{\mathbf{r}}' + \hat{\mathbf{r}}) e^{-jk(\hat{\mathbf{r}}' - \hat{\mathbf{r}}) \cdot \mathbf{v}} \quad (63)$$

the line integral on C is converted into a surface integral on the polygonal plate surface A

$$\Psi^{\text{tot}} \approx \frac{jk}{4\pi} (\hat{\mathbf{r}}' + \hat{\mathbf{r}}) \cdot \hat{\mathbf{n}} \iint_A e^{-jk(\hat{\mathbf{r}}' - \hat{\mathbf{r}}) \cdot \mathbf{v}} dA \quad (64)$$

which reduces to (44) as $\hat{\mathbf{r}} \to \hat{\mathbf{r}}'$. Note that, as illustrated in Section III.C, the vertex field, which is constitutionally of order $O(k^{-1})$, in the forward direction experiences a double transition. However, in the RCS case the transitional behavior is not described by the transition functions, which are set to unity, but by the singularity cancellation among the contributions relevant to the various vertexes, so that the final result becomes of order $O(k)$. Also note, that the weaker singularity terms neglected in (59) (i.e., from the non singular B terms in (22)) lead to a higher order field contribution, of order $O(k^0)$, whereas the non singular terms $D_m^{\text{tip},i}$ with $m > 2$, if any, provide a field of order $O(k^{-1})$. Hence (44) represents the leading term of the field asymptotic expansion. The proof reported above can be easily

repeated for an observation aspect $\hat{\mathbf{r}} = \hat{\mathbf{r}}' - 2\hat{\mathbf{n}}(\hat{\mathbf{n}} \cdot \hat{\mathbf{r}}')$, i.e., in the plate specular reflection direction, but it is omitted for the sake of brevity. Its final result is incorporated in (44).

REFERENCES

[1] R. G. Kouyoumjian and P. H. Pathak, "A uniform geometrical theory of diffraction for an edge in a perfectly conducting surface," *Proc. IEEE*, vol. 62, no. 11, pp. 1448–1461, Nov. 1974.

[2] M. Albani, F. Capolino, S. Maci, and R. Tiberio, "Diffraction at a thick screen including corrugations on the top face," *IEEE Trans. Antennas Propag.*, vol. 45, no. 2, pp. 277–283, Feb. 1997.

[3] F. Capolino, M. Albani, S. Maci, and R. Tiberio, "Double diffraction at a pair of coplanar skew edges," *IEEE Trans. Antennas Propag.*, vol. 45, no. 8, pp. 1219–1226, Aug. 1997.

[4] M. Albani, P. Piazzesi, F. Capolino, S. Maci, and R. Tiberio, "Shielding effect of a thick screen with corrugation," *IEEE Trans. Electrom. Compat.*, vol. 40, no. 3, pp. 235–239, Aug. 1998.

[5] M. Albani, "A uniform double diffraction coefficient for a pair of wedges in arbitrary configuration," *IEEE Trans. Antennas Propag.*, vol. 53, no. 2, pp. 702–710, Feb. 2005.

[6] L. Kraus and L. M. Levine, "Diffraction by an elliptic cone," *Commun. Pure Appl. Math.*, vol. 14, no. 1, pp. 49–68, 1961.

[7] R. Satterwhite, "Diffraction by a quarter plane, the exact solution, and some numerical result," *IEEE Trans. Antennas Propag.*, vol. 22, no. 3, pp. 500–503, May 1974.

[8] J. N. Sahalos and G. A. Thiele, "The eigenfunction solution for scattered fields and surface currents of a vertex," *IEEE Trans. Antennas Propag.*, vol. 31, no. 1, pp. 206–211, Jan. 1983.

[9] J. J. Bowman, T. B. A. Senior, and P. L. E. Uslenghi, *Electromagnetic and Acoustic Scattering by Simple Shapes*. New York: Hemisphere, 1987.

[10] T. B. Hansen, "Diffraction by a plane angular sector, a new derivation," *IEEE Trans. Antennas Propag.*, vol. 38, no. 11, pp. 1892–1894, Nov. 1990.

[11] S. Blume, "Spherical-multipole analysis of electromagnetic and acoustical scattering by a semi-infinite elliptic cone," *IEEE Antennas Propag. Mag.*, vol. 38, no. 2, pp. 33–44, Apr. 1996.

[12] S. Blume and V. Krebs, "Numerical evaluation of dyadic diffraction coefficients and bistatic radar cross sections for a perfectly conducting semi-infinite elliptic cone," *IEEE Trans. Antennas Propag.*, vol. 46, no. 3, pp. 414–424, Mar. 1998.

[13] L. Klinkenbush, "Electromagnetic scattering by semi-infinite circular elliptic cones," *Radio Sci.*, vol. 42, no. 6, 2007, RS6S10, doi:10.1029/2007RS003649.

[14] J. Radlow, "Diffraction by a quarter plane," *Arch. Rational Mech. Anal.*, vol. 8, no. 1, pp. 139–158, Jan. 1961.

[15] J. Radlow, "Note on the diffraction at a corner," *Arch. Rational Mech. Anal.*, vol. 19, no. 1, pp. 62–70, Jan. 1965.

[16] N. C. Albertsen, "Diffraction by a quarterplane of the field from a halfwave dipole," *IEE Proc., Microwaves Antennas Propag.*, vol. 144, no. 3, pp. 191–196, Jun. 1997.

[17] M. Albani, "On Radlow's quarter-plane diffraction solution," *Radio Sci.*, vol. 42, no. 6, 2007, RS6S11, doi:10.1029/2006RS003528.

[18] F. A. Sikta, W. D. Burnside, T. T. Chu, and L. Peters, Jr., "First-order equivalent current and corner diffraction from flat plate structures," *IEEE Trans. Antennas Propag.*, vol. 31, no. 4, pp. 584–589, Jul. 1983.

[19] K. C. Hill, "A UTD Solution to the EM Scattering by the Vertex of a Perfectly Conducting Plane Angular Sector," Ph.D. dissertation, Dept. Elect. Eng., The Ohio State Univ., Columbus, OH, 1990.

[20] K. C. Hill and P. H. Pathak, "A UTD solution for the EM diffraction by a corner in a plane angular sector," in *Proc. IEEE AP-Symp.*, London, ON, Canada, Jun. 24–28, 1991, vol. 1, pp. 2–5.

[21] T. B. Hansen, "Corner diffraction coefficients for the quarter plane," *IEEE Trans. Antennas Propag.*, vol. 39, no. 7, pp. 976–984, Jul. 1991.

[22] S. Maci, R. Tiberio, and A. Toccafondi, "Diffraction at a plane angular sector," *J. Electromagn. Wave Applicat.*, vol. 8, no. 9–10, pp. 1247–1276, Sep. 1994.

[23] F. Capolino and S. Maci, "Uniform high-frequency description of singly, doubly, and vertex diffracted rays for a plane angular sector," *J. Electromagn. Wave Applicat.*, vol. 10, no. 9, pp. 1175–1197, Oct. 1996.

[24] S. Maci, M. Albani, and F. Capolino, "ITD formulation for the currents on a plane angular sector," *IEEE Trans. Antennas Propag.*, vol. 46, no. 9, pp. 1318–1327, Sep. 1998.

[25] A. Michaeli, "Comments on "first-order equivalent current and corner diffraction scattering from flat plate structures," *IEEE Trans. Antennas Propag.*, vol. 32, no. 9, pp. 1011–1012, Sep. 1984.

[26] D. S. Jones, "A uniform asymptotic expansion of a certain double integral," *Proc. Roy Soc. Edin. (A)*, vol. 69, no. 15, pp. 205–226, 1971.

[27] P. C. Clemmow and T. B. A. Senior, "A note on a generalized Fresnel integral," *Proc. Cambridge Phil. Soc.*, vol. 49, pp. 570–572, 1953.

[28] F. Capolino and S. Maci, "Simplified, closed-form expressions for computing the generalized Fresnel integral and their application to vertex diffraction," *Microw. Opt. Techn. Lett.*, vol. 9, no. 1, pp. 32–37, May 1995.

[29] V. P. Smyshlyaev, "The high-frequency diffraction of electromagnetic waves by cones of arbitrary cross-section," *Soc Indust. Appl. Math.*, vol. 53, no. 3, pp. 670–688, Jun. 1993.

[30] V. M. Babich, V. P. Smyshlyaev, D. B. Dement'ev, and B. A. Samokish, "Numerical calculation of the diffraction coefficients for an arbitrary shaped perfectly conducting cone," *IEEE Trans. Antennas Propag.*, vol. 44, no. 5, pp. 740–747, May 1996.

[31] A. Rubinowicz, "Über Miyamoto-Wolfsche vektorpotentiale, die mit der lösung eines randwertproblems im gebiete der schwingungsgleichung verknüpft sind," *Acta Physica Polonica*, vol. 28, pp. 361–387, Mar. 1965.

[32] A. Rubinowicz, "The Miyamoto-Wolf diffraction wave," *Progr. Opt.*, vol. 4, pp. 199–240, 1965.

[33] R. Tiberio and S. Maci, "An incremental theory of diffraction: Scalar formulation," *IEEE Trans. Antennas Propag.*, vol. 42, no. 5, pp. 600–612, May 1994.

[34] S. Maci, R. Tiberio, and A. Toccafondi, "Incremental diffraction coefficients for source and observation at finite distance from an edge," *IEEE Trans. Antennas Propag.*, vol. 44, no. 5, pp. 593–599, May 1996.

[35] R. Tiberio, A. Toccafondi, A. Polemi, and S. Maci, "Incremental theory of diffraction: A new-improved formulation," *IEEE Trans. Antennas Propag.*, vol. 52, no. 9, pp. 2234–2243, Sep. 2004.

[36] W. Gordon, "Far-field approximations to the Kirchhoff-Helmholtz representations of scattered fields," *IEEE Trans. Antennas Propag.*, vol. 23, no. 4, pp. 590–592, Jul. 1975.

[37] L. P. Ivrissimtzis and R. J. Marhefka, "A uniform ray approximation of the scattering by polyhedral structures including higher order terms," *IEEE Trans. Antennas Propag.*, vol. 40, no. 11, pp. 1302–1312, Nov. 1992.

[38] R. Ianconescu and E. Heyman, "Pulsed beam diffraction by a perfectly conducting wedge: Exact solution," *IEEE Trans. Antennas Propag.*, vol. 42, no. 10, pp. 1377–1385, Oct. 1994.

[39] E. Heyman and R. Ianconescu, "Pulsed beam diffraction by a perfectly conducting wedge: Local scattering models," *IEEE Trans. Antennas Propag.*, vol. 43, no. 5, pp. 519–528, May 1995.

[40] P. R. Rousseau and P. H. Pathak, "Time-domain uniform geometrical theory of diffraction for a curved wedge," *IEEE Trans. Antennas Propag.*, vol. 43, no. 12, pp. 1375–1382, Dec. 1995.

[41] F. Capolino and M. Albani, "Time domain double diffraction at a pair of coplanar skew edges," *IEEE Trans. Antennas Propag.*, vol. 53, no. 4, pp. 1455–1469, Apr. 2005.

[42] F. Capolino and R. Tiberio, "A time domain incremental theory of diffraction (TD-ITD) for a wedge," presented at the Int. Conf. Electromagn. Adv. Applic. (ICEAA), Torino, Italy, Sep. 2001.

[43] F. Capolino and M. Albani, "Impulsive pyramid-vertex and double-wedge diffraction coefficients," presented at the IEEE AP-Symp., Boston, MA, Jul. 8–13, 2001.

Matteo Albani (M'98) was born in Florence, Italy, on January 5, 1970. He received the Laurea degree in electronic engineering and the Ph.D. in telecommunications engineering from the University of Florence, Italy, in 1994 and 1998, respectively.

From 1999 to 2001, he was an Associate Researcher with the Department of Information Engineering, University of Siena, Siena, Italy. In 2001, he joined the University of Messina, Messina, Italy, as an Assistant Professor at the College of Engineering. In 2005, he moved back to the University of Siena where he is an Adjunct Professor. His research interests encompass high-frequency methods for electromagnetic scattering and propagation, numerical methods for array antennas, antenna analysis and design.

Dr. Albani was awarded the "Giorgio Barzilai" prize for the Best Young Scientist paper at the Italian National Conference on Electromagnetics in 2002 (XIV RiNEm).

Filippo Capolino (S'94–M'97–SM'04) received the Laurea degree (*cum laude*) and the Ph.D. degree in electrical engineering from the University of Florence, Italy, in 1993 and 1997, respectively.

He is presently employed as an Assistant Professor at the Department of Electrical Engineering and Computer Science of the University of California, Irvine. He has been an Assistant Professor at the Department of Information Engineering of the University of Siena, Italy. From 1997 to 1998, he was a Fulbright Research Visitor with the Department of Aerospace and Mechanical Engineering, Boston University, MA, where he continued his research with a Grant from the Italian National Research Council (CNR), from 1998 to 1999. From 2000 to 2001 and in 2006, he was a Research Assistant Visiting Professor with the Department of Electrical and Comp. Engineering, University of Houston, TX. In November–December 2003, he was an Invited Assistant Professor at the Institut Fresnel, Marseille, France. His research interests include antennas and waveguides, metamaterials and their applications, micro and nanotechnology, sensors in both microwave and optical ranges, wireless and telecommunications systems, chip-integrated antennas, and theoretical and applied electromagnetics in general. He has been the EU Coordinator of the EU Doctoral Programmes on Metamaterials (2004–2009). He is a founder and an Editor of the new journal *Metamaterials* since 2007. He is the Editor of the *Metamaterials Handbook*, CRC-Press, 2009.

Dr. Capolino was awarded the MMET'94 Student Paper Competition Award in 1994, the Raj Mittra Travel Grant for Young Scientists in 1996, and the Raj Mittra Travel Grant for Senior Scientists in 2006, the "Barzilai" prize for the best paper at the National Italian Congress of Electromagnetism (XI RiNEm) in 1996, and a Young Scientist Award for participating at the URSI Int. Symp. Electromagnetic Theory in 1998. He received the R. W. P. King Prize Paper Award from the IEEE Antennas and Propagation Society for the Best Paper of the Year 2000, by an author under 36. He is a coauthor of the "Fast Breaking Papers, October 2007" in EE and CS, about metamaterials (paper that had the highest percentage increase in citations in Essential Science Indicators, ESI). From 2002 to 2008, he served as an Associate Editor for the IEEE TRANSACTIONS ON ANTENNAS AND PROPAGATION.

Giorgio Carluccio was born in 1979 and grew up in Ortelle, Lecce, Italy. He received the Laurea degree in telecommunications engineering from the University of Siena, Siena, Italy, in 2006, where he is currently working towards the Ph.D. degree.

From October 2008 to March 2009, he was an invited Visiting Scholar with the ElectroScience Laboratory, Department of Electrical and Computer Engineering, The Ohio State University, Columbus. His research interests are focused on asymptotic high-frequency methods for electromagnetic scattering and propagation, complex sources, and Gaussian beams.

Stefano Maci (F'04) was born in Rome in 1961. He received the Laurea degree (*cum laude*) in electronic engineering from the University of Florence, Italy, in 1987.

In 1998, he joined the University of Siena, Italy, where he presently is a Full Professor. He was a coauthor of an *Incremental Theory of Diffraction* for the description of a wide class of electromagnetic scattering phenomena at high frequency, and of a diffraction theory for the high frequency analysis of large truncated periodic structures. His research interests include: theory of electromagnetism, integral equation methods, large phased array antennas, planar antennas and multilayer structures, reflector antennas and feed horns, metamaterials. In 2004, he was the founder, and he presently is the Director, of the "European school of antennas" (ESoA), a post graduate school comprising 26 courses and about 150 teachers coming from 20 European research centers. He was the responsible of several projects funded by the European Union (EU), by the European Space Agency (ESA-ESTEC) and by various European industries; he was WP leader in the Network of Excellence "Antenna Center of Excellence" (FP6, EU). He is principal author or coauthor of about 100 papers published in international journals, eight book chapters, and about 300 papers in proceedings of international conferences.

Prof. Maci was awarded the Best Paper Award several times from international journals and at conferences. He was an Associate Editor of the IEEE TRANSACTIONS ON ELECTROMAGNETIC COMPATIBILITY and twice the Guest Editor of special issues of the IEEE TRANSACTIONS ON ANTENNAS AND PROPAGATION. He is an Associate Editor of the IEEE TRANSACTIONS ON ANTENNAS AND PROPAGATION. He is member of the Technical Advisory Board of the URSI Commission B, member of a NATO panel on metamaterials and MEMS, member of the scientific board of the Italian Society of Electromagnetism (SIEM), and coordinator of the board of the Italian Ph.D. school of Electromagnetism. He is member of Board of Directors of the European Association on Antennas and Propagation (EuRAAP). He has been an invited speaker at many international conferences, and presenter of various short courses about EBG material, high-frequency methods, and computational methods.